On Propagation Loss for Reconfigurable Surface Wave Communications

Zhiyuan Chu, Wee Kiat New, *Member, IEEE,* Kin-Fai Tong, *Fellow, IEEE,* Kai-Kit Wong, *Fellow, IEEE,* Haizhe Liu, Chan-Byoung Chae, *Fellow, IEEE,* and Yangyang Zhang

***Abstract*—Surface wave communication (SWC) is an emerging technology garnering significant interest for its diverse potential applications in communications. However, accurately computing electromagnetic field strength, which is related to the path loss, in reconfigurable surface structures, particularly for long-distance transmission, presents an ongoing challenge. To address this, we introduce a novel analytical model employing surface wave ray tracing. Unlike conventional simulations, our analytical approach enables precise computation of the electromagnetic field strength attenuation in both short and long-distance transmissions, providing invaluable insights for practical SWC implementations. Our proposed model takes into account key system parameters such as surface material, thickness, cavity porosity, and other variables influencing propagation performance. This facilitates analysis of optimal reconfigurable structures. Simulation results validate the model's accuracy in short-distance transmission, thereby endorsing its effectiveness in studying surface wave path loss over longer distances. Furthermore, our study demonstrates the SWC superiority over traditional coaxial cable and space-wave communication in mitigating path loss. Additionally, we explore the impacts of various factors such as different dielectric layers, wall materials, leakage, and pathway width on SWC performance, providing deeper insights into designing optimal reconfigurable structures for SWC applications.**

***Index Terms*—Surface wave communications, reconfigurable communication surfaces, and path loss.**

I. Introduction

As FIFTH-generation (5G) networks have been deployed globally, the journey toward sixth-generation (6G) networks has begun. 6G aims to deliver not only immense data rates, hyper-reliability, low latency, and massive connectivity but also ubiquitous connectivity, advanced sensing capabilities, integrated intelligence and etc. To achieve some or all of these goals, reconfigurable intelligent surfaces (RISs) have been investigated by academia and industry due to their capability to smartly reconfigure the wireless environment and provide substantial gains [1]. However, RISs are prone to the double path loss effect [2]. To mitigate this drawback, surface wave communication (SWC) can be an appealing solution [3].

Surface wave refers to an electromagnetic wave that propagates steadily along the surface of a planar conductor coated with a dielectric medium [4]. Technically speaking, a higher surface impedance allows the surface wave to tightly adhere to the surface in a two-dimensional (2D) propagation mode without radiation, as illustrated in Fig. 1. As a special solution for cylindrical waves, the electric field (E-field) attenuation of surface waves and their path loss are both proportional to the propagation distance, specifically $\propto \sqrt{d}$ and $\propto d$, respectively, whereas the path loss of free-space waves is proportional to the square of the distance, i.e., $\propto d^2$ [5]. Consequently, the stable, low-loss propagation along surfaces motivates the widespread application of surface waves in various domains, including wireless communications and others [3].

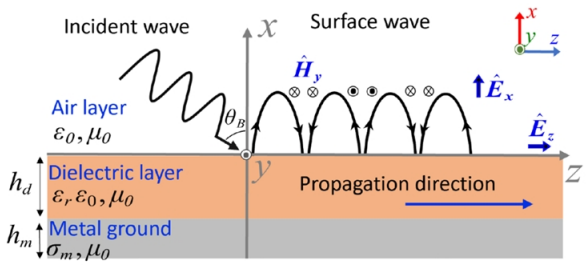

Fig. 1. Illustration of the surface wave excitation by an incident wave with Brewster's angle on a dielectric-metal surface.

Surface waves have been proposed as a viable solution for achieving high-speed communication and data transmission in Network-on-Chip (NoC) systems. By integrating multiple micro-antenna units on the chip, surface waves can be utilized to establish flexible and stable communication paths between nodes [6], [7]. In the rapidly growing field of wearable devices, electromagnetic wave propagation is also increasingly directed towards establishing more stable propagation paths directly on clothing surfaces. The use of surface wave antennas has the potential to enhance information transmission and reception between the human body and the surrounding environment [8], offering novel solutions for smart health monitoring, Internet of Things (IoT), and personal communication.

Furthermore, the emergence of surface wave-enabled liquid antennas has also been proposed for 6G networks [9], [10]. Specifically, surface wave can be adopted as a technology to flexibly connect dynamic-position radiating elements to the radio-frequency chains, thereby offering additional degrees of freedom to wireless communication systems [11], [12], [13]. This antenna technology also holds potential applications in communication, radar, and wireless sensing [13]. Additionally, in industrial environments, surface waves are being explored as an alternative to cables to reduce overall lifecycle costs. Utilizing surface waves for signal and energy transmission

The work of Z. Chu, W. K. New, K. K. Wong, K. F. Tong, and H. Liu is supported by the Engineering and Physical Sciences Research Council (EPSRC) under Grant EP/V052942/1. The work of C.-B. Chae is supported by the IITP grant funded by the Ministry of Science and ICT (MSIT), Korea (No. 2024-00428780, No. 2021-0-00486).

Z. Chu, W. K. New, K. K. Wong, K. F. Tong, and H. Liu are with the Department of Electronic and Electrical Engineering, University College London, Torrington Place, WC1E 7JE, United Kingdom. K. K. Wong is also affiliated with Yonsei Frontier Lab, Yonsei University, Seoul, Korea.

C.-B. Chae are with School of Integrated Technology, Yonsei University, Seoul, 03722, Korea.

Y. Zhang is with Kuang-Chi Science Limited, Hong Kong SAR, China.

Corresponding author: K. K. Wong (e-mail: kai-kit.wong@ucl.ac.uk).

in industrial equipment and systems can lower the use and maintenance costs associated with cables, while enhancing system reliability and flexibility [14].

The study of surface waves spans a lengthy history, with early research exploring a variety of surfaces including on planar surfaces [15], corrugated surfaces [16], elastic surfaces [17], stepped surfaces [18], and curved surfaces [19]. In recent years, attention has shifted towards metasurfaces which offers the unique capability of manipulating surface waves effectively. Metasurfaces, designed with subwavelength structured units, provide control over crucial parameters such as phase, amplitude, and polarization. These parameters significantly influence the propagation direction, scattering behavior, and refraction characteristics of surface waves [20], [21], [22].

Metasurfaces can be categorized into two types: isotropic and anisotropic [23], [24], [25]. Anisotropic metasurfaces using specific materials, can effectively minimize the scattering losses of surface waves occurring at sharp angles in physical environments [26], [27]. On the other hand, isotropic periodic metasurfaces printed on grounded dielectric substrates enable nearly perfect conversion of incident space waves into surface waves [28], [29], [30]. By controlling the surface properties, it is also possible to achieve perfect conversion from transverse magnetic (TM) surface waves to leaky waves, realizing ideal leaky wave antennas and similar devices [31].

Conversely in the opposite direction, metasurfaces can be employed to convert surface waves into space waves [32]. Moreover, three-dimensional (3D) frequency-selective surfaces with periodic rectangular frameworks can be used as planar filters for surface waves, effectively restricting the transmission channels of surface waves. This structure supports the propagation of parallel-polarized surface waves in specific channels within a desired frequency range, exhibiting an excellent band-pass frequency response [33]. Therefore, metasurfaces offer significant potential for achieving directed propagation, suppressing scattering, transforming wave characteristics, and enabling frequency selectivity of surface waves.

Inspired by these advantages, [3], [19] outlined the applications of surface waves for both indoor and outdoor environments. Specifically, metasurfaces were proposed as efficient media for converting between space waves and surface waves. For outdoor environments, the deployment of metasurfaces on buildings was suggested to readily capture space waves from the environment and convert them into surface waves. These surface waves are then guided along predetermined pathways and reconverted back into space waves to beamform toward specific users. This approach offers substantial compensation for severe double path loss effect and propagation paths that are blocked by obstacles [19]. For indoor environments, metasurfaces could be utilized in a similar manner by strategically placing them to facilitate multiple reflections of wireless signals and propagation through surfaces, thereby simultaneously enhancing signal strength and reducing interference [3].

Besides, a reconfigurable surface wave platform has recently been proposed in [34]. This platform utilizes liquid metal, such as Galinstan, to generate highly efficient and adaptive pathways for surface wave transmission. Additionally, a perforated surface has been considered, in which electrical small size cavities are uniformly distributed and can be selectively filled with liquid metal through digitally controlled pumps [35]. Despite the increasing popularity of technology for intelligently manipulating surface waves, an analytical model to compute the electromagnetic variation of the surface waves, including the effects of distance, surface materials, thickness, and other variables, is missing in the lterature.

Thus far, existing research has not provided any method to directly assess the loss of surface waves, both inside and outside of the guided pathway. The implications of multiple signal propagation phenomena, such as reflection, refraction, and attenuation, further complicate this issue. Consequently, studying surface waves in the context of wireless communications is very challenging, if not impossible, because the characteristics of surface waves are not well understood.

To overcome this challenge, we propose a novel analytical model utilizing the multi-ray tracing method. Surface wave ray tracing is a method that calculates the propagation of light rays in the environment [36]. It can be adopted to analyze the multipath effects and attenuation under various environmental conditions and optimize the performance of communication systems. In this paper, we consider the propagation of Zenneck surface waves on a flat surface, focusing on the propagation paths and field strength superposition of surface wave rays in a metal wall pathway. Zenneck surface waves are characterized by their ability to concentrate energy on the surface through impedance adjustment of the medium, achieving low losses and high propagation efficiency [4], [37]. The main contributions of this paper can be summarized as follows:

- By utilizing the multi-ray tracing method, we propose a novel analytical model for expressing the surface wave electromagnetic field. Unlike conventional simulations, our model provides analytical insights into the relationship between surface wave E-field strength attenuation and propagation distance both inside and outside the guided pathway. This capability facilitates performance analysis in future research endeavors for SWC.
- We validate the accuracy of the proposed model through 3D computer simulation technology (CST) simulations at the millimeter scale. Compared to CST simulations, our model significantly expedites the path loss computation. As such, the proposed model can be effectively applied to long-distance transmission at the meter scale, which is otherwise computationally infeasible through simulations. The application to long-distance transmission enables us to quantitatively demonstrate the superiority of SWC over coaxial cable and space-wave communication.
- Moreover, our proposed model comprehensively accounts for various critical parameters, including different dielectric layers, wall materials, and path widths, all of which influence propagation performance. This ensures a high degree of accuracy in our analyses. As demonstrated later in this paper, the numerical results closely match the simulation results, indicating that our model can reliably provide accurate insights into optimal reconfigurable structures for SWC applications.
- Analyzing the electromagnetic wave behavior in metal pin walls is highly complex. Nevertheless, our proposed

model can accurately predict the E-field strength of the metal pin configurations, serving as a robust reference for evaluating surface wave performance on reconfigurable surfaces. This is extremely beneficial as metal pin walls recently show significant potential in reconfigurable surfaces, where fluid metals can be dynamically injected into metal cavities to alter the direction of surface waves.

The remainder of this paper is organized as follows. Section II introduces the proposed analytical model for SWC. Section III then discusses the numerical and simulation results, and the conclusion is presented in Section IV.

II. Analytical Model for SWC

Here, we present the analytical model based on the surface wave ray tracing method. Specifically, we discuss the geometry of the straight guided pathway, the signal superposition within the guided pathway, and outside the guided pathway.

A. The Geometry of Straight Guided Pathway

In this paper, we propose an analytical model to calculate the theoretical power distribution at predefined measurement points. This model helps evaluate the path loss experienced by surface waves along a designated pathway.[1] To facilitate the mathematical analysis, the pathway is conceptually simplified by replacing the columns of cylindrical metal pins with two complete metal walls [38], as depicted in Fig. 2.[2] This simplification concentrates the propagation of surface waves along the guided pathway and restricts the surface wave propagation spreading beyond the boundaries of the pathway.

Our investigation is primarily concerned with the interface between the air and dielectric layer, i.e., the yz-plane where $x = 0$. The center endpoint of Transducer 1, serving as the source of the surface waves, is positioned at the origin $(0, 0, 0)$ in the xyz-coordinate system. Within the pathway, a targeted measured point is assumed to be located at the coordinate $(0, y_0, z_0)$. Moreover, two parallel columns of metal walls are embedded in the dielectric-metal surface, extending along the $+z$-direction and aligning parallel to the transducer. These walls are modeled as metal plates with an electrical conductivity of σ_w, a length of l_w, and a width of w_w. The bottom of the metal walls maintains contact with the metal ground. The separation between these two metal walls, denoted as w_p, defines the width of the guided pathway. To ensure that extraneous boundary conditions do not impact the electromagnetic field strength at the air-dielectric layer interface, the height of the metal walls is slightly higher than that of the dielectric layer. Additionally, the left initial ends of the metal walls are aligned with the $y = 0$ axis, eliminating any gaps between the metal walls and the emission aperture of the transducer along the $+z$-direction. This effectively prevents additional leakage of surface waves from gaps.

[1]For clarity, this paper refers to 'path' as the trajectory of the surface wave ray excited by the transducer from the source point to the measured point, while 'pathway' refers to the specific channel created by the guided metal walls for surface wave propagation.

[2]As verified later in this paper, such simplification is possible since the propagation of metals pins and metal walls are similar.

The surface wave rays are emitted from Transducer 1 at $(0, 0, 0)$. Theoretically, these rays propagate outward in the yz-plane, forming a semi-circular region centered around the transducer as they extend from the source point. The path travelled by the surface wave ray from the source to the measured point, representing the propagation trajectory, is denoted as path $m \in \mathbf{N}^+$. In this model, there are infinitely many paths, and thus m ranges from 1 to $+\infty$. As shown in Fig. 2(a), there exists a direct surface wave path between the source point and the measured point, resembling a line-of-sight path. This unique path, identified as path 1, stands out because the remaining paths require reflection between the two metal walls to reach the measured point. For example, considering a single reflection, the surface waves in path 2 and path 3, originating from the source point, will reflect at the inner sides of the upper and lower metal walls, respectively, at reflection points A and B, before reaching the measured point.

Fig. 2(b) depicts the surface wave rays of paths 1-3 within the two layers of metal walls, illustrating the distribution of the field strengths. As the surface wave propagation direction in each path is not solely in the $+z$-direction anymore, the surface wave equation in [39] for the field strengths needs to be re-derived accordingly. Here, the E-field component $\hat{\boldsymbol{E}}_{\boldsymbol{p}}$ is defined as the component along the direction of propagation, while $\hat{\boldsymbol{H}}_{\boldsymbol{v}}$ represents the H-field component. It is worth noting that the direction of $\hat{\boldsymbol{E}}_{\boldsymbol{x}}$ remains unchanged as it stays aligned with the $+x$-direction. Consequently, for any surface wave in path m, their field strengths can be rewritten as

$$\begin{cases} \hat{\boldsymbol{H}}_{\boldsymbol{v}} = \hat{\boldsymbol{v}} \dfrac{1}{\sqrt{d_m}} A e^{-\gamma_p d_m} e^{-\gamma_x x} e^{j\omega t} Q_m, \\ \hat{\boldsymbol{E}}_{\boldsymbol{x}} = \hat{\boldsymbol{x}} \dfrac{\gamma_p}{\sqrt{d_m} j\omega\varepsilon_0} A e^{-\gamma_p d_m} e^{-\gamma_x x} e^{j\omega t} Q_m, \\ \hat{\boldsymbol{E}}_{\boldsymbol{p}} = -\hat{\boldsymbol{p}} \dfrac{\gamma_x}{\sqrt{d_m} j\omega\varepsilon_0} A e^{-\gamma_p d_m} e^{-\gamma_x x} e^{j\omega t} Q_m, \end{cases} \tag{1}$$

where d_m represents the surface wave ray propagation distance in each path m and A is an initial amplitude constant, which can be set as 1 for ease of calculations. Furthermore, $\hat{\boldsymbol{v}}$, $\hat{\boldsymbol{x}}$, and $\hat{\boldsymbol{p}}$ denote the corresponding unit vectors for the field strengths. The parameters γ_p and γ_x represent the propagation coefficient along the direction of wave propagation and the $+x$-direction, respectively, while $e^{j\omega t}$ is the complex exponential function and can be omitted in subsequent derivations. It should be noted that Q_m is defined as a set of factors that account for the influence of multiple reflections along path m from the source to the measured point on the values of field strengths.

As seen in Fig. 2(c), the surface wave rays of the direct path 1 and the reflected paths 2 and 3, each with different phases and magnitudes, converge at the measured point and undergo superposition of field strengths. Here, $\hat{\boldsymbol{k}}_1$, $\hat{\boldsymbol{k}}_2$ and $\hat{\boldsymbol{k}}_3$ represent the direction of the wave vector. In general, the magnitude of $\hat{\boldsymbol{E}}_{\boldsymbol{x}}$ is much larger than that of $\hat{\boldsymbol{E}}_{\boldsymbol{p}}$, which is determined by the values of γ_p and γ_x. Therefore, in the ray tracing model and simulations, the power of $\hat{\boldsymbol{E}}_{\boldsymbol{x}}$ in dB can be considered as the power of the surface wave. Furthermore, since the field strength of $\hat{\boldsymbol{E}}_{\boldsymbol{x}}$ always aligns with the x-axis rather than varying in the yz-plane like $\hat{\boldsymbol{E}}_{\boldsymbol{p}}$ and $\hat{\boldsymbol{H}}_{\boldsymbol{v}}$ with respect to path m, we focus on the superposition of $\hat{\boldsymbol{E}}_{\boldsymbol{x}}$. This

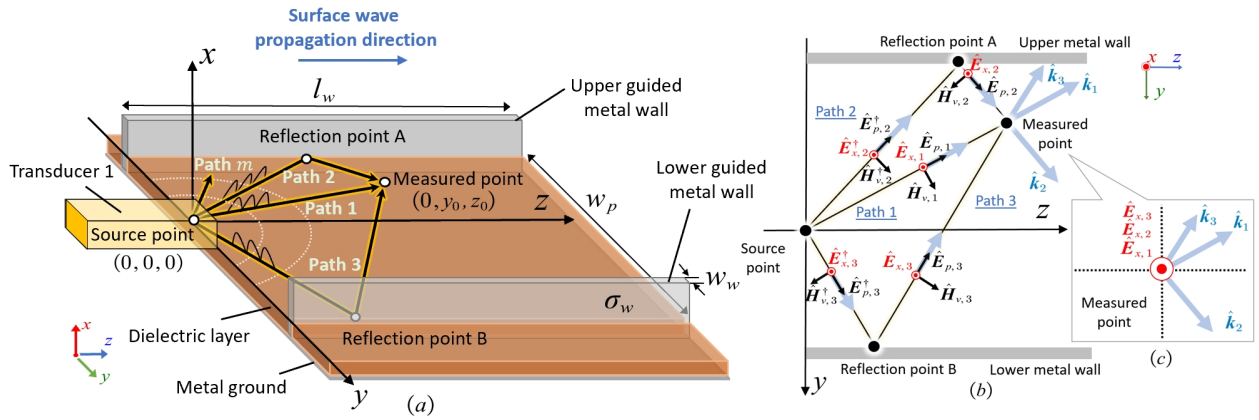

Fig. 2. (a) The geometry of the straight guided pathway created by two complete metal walls embedded into the surface for analyzing the surface wave rays in different propagation paths from the source point $(0,0,0)$ to the measured point $(0,y_0,z_0)$; (b) The distribution of the field strengths of surface wave rays in paths 1-3 within the two layers of metal walls; (c) Their $\hat{\boldsymbol{E}}_{\boldsymbol{x}}$ at the measured point.

simplifies the mathematical analysis as the vector notation can be omitted, and E_x can be treated as a scalar directly.

B. Signal Superposition Inside the Pathway

The number of reflections experienced by the propagation path is denoted as $n \in \mathbf{N}$. Fig. 3 illustrates several examples of paths ranging from $n=0$ to $+\infty$ in the yz-plane. Let w_1 and w_2 represent the distances from the source point $(0,0)$ to the lower and upper metal walls, respectively, where $w_1 + w_2 = w_p$. As mentioned earlier, there is only one line-of-sight path between the source and the measured points that undergoes no reflection. Therefore, when $n=0$, only path 1 exists. The propagation distance of path 1 can be computed as $d_1 = \sqrt{y_0^2 + z_0^2}$, given that the coordinates of the source and the measured points projected onto the yz-plane are $(0,0)$ to (y_0,z_0), respectively, as shown in Fig. 3(a).

When $n \geq 1$, there are exactly two distinct paths labeled as $2n$ and $2n+1$, as further depicted in Figs. 3(b)–3(f). For example, when $n=1$, only paths 2 and 3 are present, and when $n=2$, only paths 4 and 5 exist. This pattern continues for higher values of n due to the fixed incident angles θ_{2n} and θ_{2n+1} associated with path $2n$ and path $2n+1$, respectively. Furthermore, each of these paths has a specific propagation distance. Using trigonometry, we can conclude that for any integer value $n \geq 1$, the incident angles and propagation distances of paths $2n$ and $2n+1$ can be derived as (2) and (3), respectively (see bottom of next page).

In (2) and (3), the notation 'mod' represents the modulo operation. The incident angles θ_{2n} and θ_{2n+1} are constrained to the range $(0, \frac{\pi}{2})$. Note that as n approaches infinity, these incident angles, θ_{2n} and θ_{2n+1}, approach infinitesimally small values, while the propagation distances, d_{2n} and d_{2n+1}, approach infinity. Fig. 3(f) illustrates the distribution of the incident and reflected E-field and H-field components of the surface wave ray on the metal wall during a single reflection.

By applying the boundary conditions, the reflection coefficient of the TM mode surface wave can be derived as

$$R\left(\theta_m, \sigma_w\right) = \frac{\cos\theta_m - \sqrt{\varepsilon_w/\varepsilon_0 - \sin^2\theta_m}}{\cos\theta_m + \sqrt{\varepsilon_w/\varepsilon_0 - \sin^2\theta_m}}, \tag{4}$$

where $\varepsilon_w = -j\frac{\sigma_w}{\omega}$, θ_m is the common incident angle, and ε_w denotes the permittivity of the metal walls, which is defined by its electrical conductivity σ_w. We can see that the reflection coefficient, $R\left(\theta_m, \sigma_w\right)$, is primarily dependent on the incident angle and the electrical conductivity of metal walls.

As discussed earlier, the surface wave rays are excited from the source point, forming a semi-circular region centered around the transducer. The field strength of the surface wave ray varies with different propagation directions, i.e., $\frac{\pi}{2} - \theta_m$. The magnitude of the variation can be computed as [41]

$$C\left(\theta_m\right) = \cos\frac{9w_a\left(\pi - 2\theta_m\right)}{14\lambda}, \tag{5}$$

where λ denotes the wavelength of operating frequency and w_a denotes the aperture width of a rectangular transducer.

As a result, the E_x in (1) at the measured point (y_0,z_0) can be reformulated within this model by considering multiple surface wave rays. For $n=0$, $E_{x,1}$ exists in path 1. For $n \geq 1$, $E_{x,2n}$ and $E_{x,2n+1}$ exist in path $2n$ and path $2n+1$, respectively. Furthermore, the set factor $Q_m = R^n\left(\theta_m, \sigma_w\right) C\left(\theta_m\right)$ should be taken into account, which leads to

$$\begin{cases} E_{x,1} &= A\dfrac{\gamma_p}{j\omega\varepsilon_0}\dfrac{1}{\sqrt{d_1}} C\left(\theta_1\right) e^{-\gamma_p d_1} e^{-\gamma_x x}, & n=0 \\ E_{x,2n} &= A\dfrac{\gamma_p}{j\omega\varepsilon_0}\dfrac{1}{\sqrt{d_{2n}}} C\left(\theta_{2n}\right) \\ & \quad \times R^n\left(\theta_{2n}, \sigma_w\right) e^{-\gamma_p d_{2n}} e^{-\gamma_x x}, & n \geq 1 \\ E_{x,2n+1} &= A\dfrac{\gamma_p}{j\omega\varepsilon_0}\dfrac{1}{\sqrt{d_{2n+1}}} C\left(\theta_{2n+1}\right) \\ & \quad \times R^n\left(\theta_{2n+1}, \sigma_w\right) e^{-\gamma_p d_{2n+1}} e^{-\gamma_x x}, & n \geq 1, \end{cases} \tag{6}$$

where $R^n\left(\theta_m, \sigma_w\right)$ gives the cumulative impact of n successive reflections on the surface wave ray within the walls.

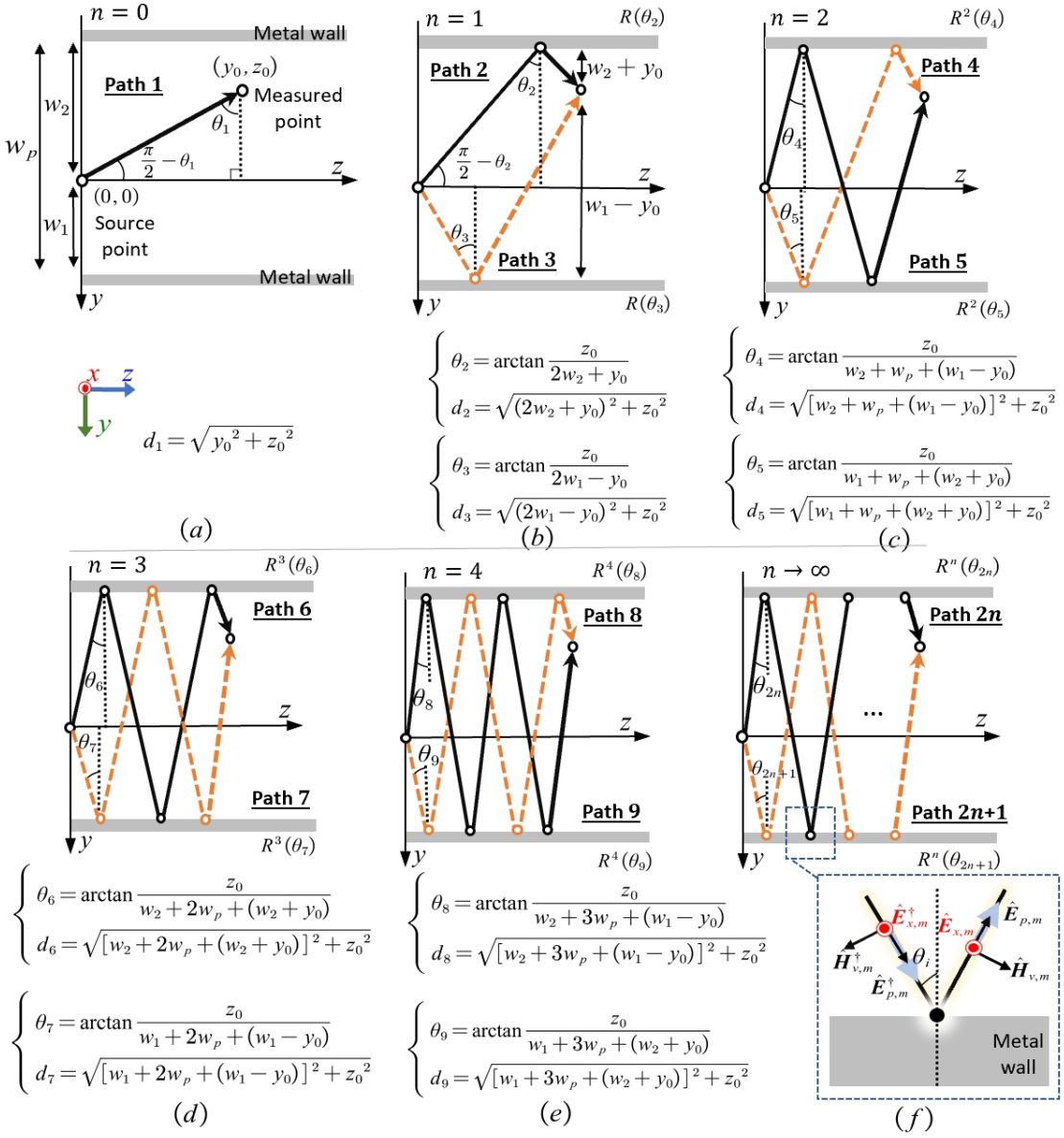

Fig. 3. The illustration of the surface wave rays in propagation paths within the metal wall after (a) 0, (b) 1, (c) 2, (d) 3, (e) 4 and (f) n times reflection and its E-field and H-field components distribution at a reflection point.

$$\begin{cases} \theta_{2n} = \arctan\left(\dfrac{z_0}{w_2 + (n-1)\,w_p + (n \bmod 2)\,(w_2 + y_0) + (n-1 \bmod 2)\,(w_1 - y_0)}\right) \\ d_{2n} = \sqrt{\left[w_2 + (n-1)\,w_p + (n \bmod 2)\,(w_2 + y_0) + (n-1 \bmod 2)\,(w_1 - y_0)\right]^2 + z_0^2}\,, \quad n \geq 1\,, \end{cases} \tag{2}$$

$$\begin{cases} \theta_{2n+1} = \arctan\left(\dfrac{z_0}{w_1 + (n-1)\,w_p + (n-1 \bmod 2)\,(w_2 + y_0) + (n \bmod 2)\,(w_1 - y_0)}\right) \\ d_{2n+1} = \sqrt{\left[w_1 + (n-1)\,w_p + (n-1 \bmod 2)\,(w_2 + y_0) + (n \bmod 2)\,(w_1 - y_0)\right]^2 + z_0^2}\,, \quad n \geq 1\,, \end{cases} \tag{3}$$

Furthermore, the cumulative E-field strength at the measured point, i.e., $E_{x,c}$, is a superposition of the $E_{x,m}$ for all the rays that arrive at the measured point through different paths m. Therefore, $E_{x,c}$ can be modeled as

$$E_{x,c} = E_{x,1} + \sum_{n=1}^{\infty} \left(E_{x,2n} + E_{x,2n+1} \right). \tag{7}$$

Recall that as n approaches positive infinity, the incident angles, θ_{2n} and θ_{2n+1}, become infinitely small, while the propagation distances, d_{2n} and d_{2n+1}, become infinitely large, as evident in (2) and (3). These infinitely large propagation distances give rise to an infinite decay in path loss, causing the E-field values to diminish significantly and become negligible. Consequently, $E_{x,c}$ will converge to a specific value.

To derive the relationship between the propagation distance, d, and the cumulative E-field strength, $E_{x,c}$, we consider the scenario where the source and measured points are both positioned along a line, which is midway between the two metal walls. In other words, we have $w_1 = w_2 = \frac{w_p}{2}$, $y_0 = 0$, and $z_0 = d_1 = d$. By substituting these values into (2) and (3), we can obtain the incident angle and distance as

$$\begin{cases} \theta_{2n} = \theta_{2n+1} = \arctan\left(\dfrac{d}{\sqrt{n^2 w_p^2 + d^2}} \right), \\ d_{2n} = d_{2n+1} = \sqrt{n^2 w_p^2 + d^2}. \end{cases} \tag{8}$$

Substituting (6) and (8) into (7), the cumulative E-field strength can be obtained as

$$\begin{aligned} E_{x,c} &= E_{x,1} + 2\sum_{n=1}^{\infty} E_{x,2n} \\ &= A\frac{2\gamma_p}{j\omega\varepsilon_0} \left[\frac{1}{2\sqrt{d}} e^{-\gamma_p d} + \sum_{n=1}^{\infty} \frac{1}{\sqrt[4]{n^2 w_p^2 + d^2}} \right. \\ &\times C\left(\arctan\left(\frac{d}{\sqrt{n^2 w_p^2 + d^2}} \right) \right) e^{-\gamma_p \sqrt{n^2 w_p^2 + d^2}} \\ &\left. \times R^n \left(\arctan\left(\frac{d}{\sqrt{n^2 w_p^2 + d^2}} \right), \sigma_w \right) \right] e^{-\gamma_x x}. \end{aligned} \tag{9}$$

As seen in (9), the accumulated E-field strength at the considered measurement point is closely related to the propagation distance d. In particular, a larger d implies a smaller E-field along each path, leading to a reduced total accumulated E-field strength. Furthermore, we can observe the characteristics of the propagating surface and the relationship with the E-field strength. For instance, a wider pathway width, w_p, results in decreased cumulative strength, indicating higher energy dispersion and a lower power spectral density per unit space. On the other hand, greater electrical conductivity of metal walls corresponds to a higher E-field within the pathway.

C. Signal Superposition Outside the Pathway

The signal of surface waves outside the metal walls can also be calculated using the proposed analytical ray tracing model. Fig. 4(a) illustrates the placement of the measured point (y_0, z_0) outside the walls, where it is observed that the surface wave ray in path 1 directly traverses the lower metal wall from the source point to reach the measured point. In Fig. 4(b), the ray in path 2 undergoes single reflection at the wall and continues its propagation to reach the measured point. Note that $n \in \mathbf{N}$ is similarly defined as the number of reflections, and Figs. 4(c)–4(f) provide the equations of the incident angles and propagation distances for different surface wave paths.

In contrast to the scenario within the metal walls discussed in the previous section, it is important to emphasize that outside the metal walls, each value of n corresponds to only a single propagation path, rather than two, due to its unique trigonometric properties. Fig. 4(f) presents the distribution of the E-field and H-field components at the transmission point on the wall. It can be observed that the incident surface wave undergoes two refractions before traversing the metal wall to reach the measured point. The transmission coefficients for the two refractions can be denoted as T_1 and T_2. Note that the width of the wall, denoted as w_w, is usually much smaller than the wavelength. Hence, its influence on practical calculations of propagation distance is negligible. As a result, the incident angle and propagation distance can be obtained as

$$\begin{cases} \theta'_{n+1} = \arctan\left(\dfrac{z_0}{y_0 + n w_p} \right) \\ d'_{n+1} = \sqrt{(y_0 + n w_p)^2 + z_0^2}, \quad n \geq 0. \end{cases} \tag{10}$$

As shown in Fig. 4(f), the transmission angle θ_t can be determined using Snell's law, given by

$$\theta_t = \arcsin\left(\sqrt{\frac{\varepsilon_0}{\varepsilon_w}} \sin\theta'_m \right). \tag{11}$$

Based on the electromagnetic boundary conditions, the transmission coefficients T_1 and T_2 can be obtained as

$$\begin{cases} T_1\left(\theta'_m, \sigma_w\right) = \dfrac{2\cos\theta'_m}{\cos\theta'_m + \sqrt{\frac{\varepsilon_w}{\varepsilon_0} - \sin^2\theta'_m}} \\ T_2\left(\theta'_m, \sigma_w\right) = \dfrac{2\cos\theta_t}{\cos\theta_t + \sqrt{\frac{\varepsilon_0}{\varepsilon_w} - \sin^2\theta_t}}. \end{cases} \tag{12}$$

It can be observed that both T_1 and T_2 can be written as equations involving the incident angle θ'_m and the electrical conductivity of the metal walls σ_w. Consequently, the equation for $E'_{x,m}$ in path $n+1$ at the measured point, after n reflections and two refractions, can be expressed as

$$\begin{aligned} E'_{x,n+1} &= A\frac{\gamma_p}{j\omega\varepsilon_0} \frac{1}{\sqrt{d'_{n+1}}} C\left(\theta'_{n+1}\right) \\ &\times R^n\left(\theta'_{n+1}, \sigma_w\right) T_1\left(\theta'_{n+1}, \sigma_w\right) \\ &\times T_2\left(\theta'_{n+1}, \sigma_w\right) e^{-\gamma_p d'_{n+1}} e^{-\gamma_x x}, \quad n \geq 1. \end{aligned} \tag{13}$$

The cumulative E-field strength $E'_{x,c}$ for all the rays that arrive at the measured point along different paths is written as

$$E'_{x,c} = \sum_{n=0}^{\infty} E'_{x,n+1}. \tag{14}$$

In Fig. 4(a), θ_0 is defined as the tilted angle included between the z-axis and the line connecting the source and target points.

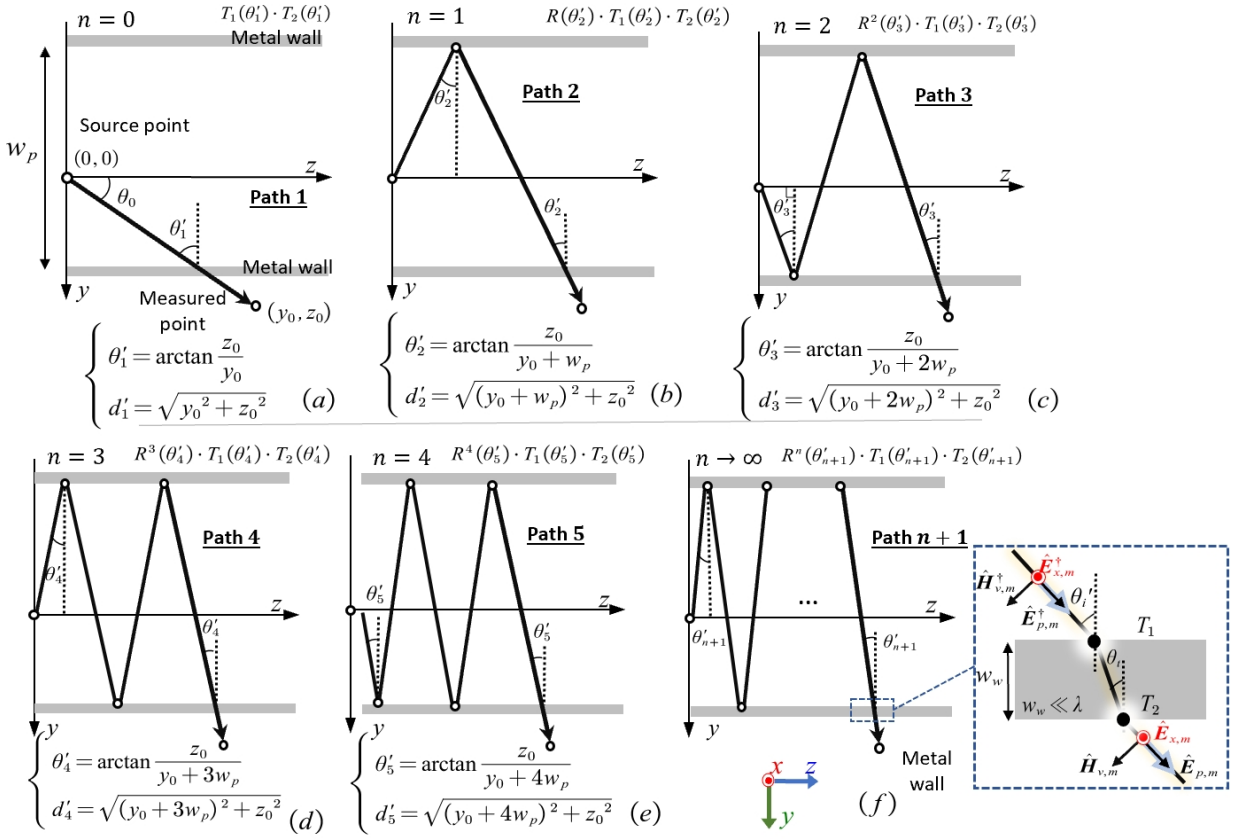

Fig. 4. The illustration of the transmitting surface wave rays in propagation paths outside the metal wall after (a) 0, (b) 1, (c) 2, (d) 3, (e) 4 and (f) n times reflection and its E-field and H-field components distribution at a transmission point.

Subsequently, the values $z_0 = d\cos\theta_0$ and $y_0 = d\sin\theta_0$ can be substituted into (12) and (13). By simplifying the E-field strength in (14), we obtain

$$\begin{aligned} E'_{x,c} &= \sum_{n=0}^{\infty} E'_{x,n+1} \\ &= A\frac{\gamma_p}{j\omega\varepsilon_0}\sum_{n=0}^{\infty} \frac{1}{\sqrt[4]{(d\sin\theta_0+nw_p)^2+d^2\cos^2\theta_0}} \\ &\times C\left(\arctan\left(\frac{d\cos\theta_0}{d\sin\theta_0+nw_p}\right)\right) \\ &\times R^n\left(\arctan\left(\frac{d\cos\theta_0}{d\sin\theta_0+nw_p}\right),\sigma_w\right) \\ &\times T_1\left(\arctan\left(\frac{d\cos\theta_0}{d\sin\theta_0+nw_p}\right),\sigma_w\right) \\ &\times T_2\left(\arctan\left(\frac{d\cos\theta_0}{d\sin\theta_0+nw_p}\right),\sigma_w\right) \\ &\times e^{-\gamma_p\sqrt{(d\sin\theta_0+nw_p)^2+d^2\cos^2\theta_0}}e^{-\gamma_x x}. \end{aligned} \tag{15}$$

By inspecting (15), we can observe that the value of $E'_{x,c}$ along the path outside the measurement point is also influenced by the propagation distance d. Similarly, a larger d leads to a reduced total accumulated E-field strength. The width of the pathway, w_p, affects the E-field strength, as it increases the path length, thereby causing greater attenuation and resulting in reduced cumulative E-field. In contrast, higher electrical conductivity of metallic walls increases the E-field outside the pathway. A comparison of the E-field between the interior and exterior paths will be discussed in subsequent results.

III. Results and Discussion

In this section, we provide the 3D electromagnetic simulation results using the CST software to validate the derived expressions for E_x. The simulations are conducted at an operating frequency of 26 GHz, and we use WR-34 rectangular waveguides with dimensions of height $h_a = 4.318\,\text{mm}$ and width $w_a = 8.636\,\text{mm}$ as the transducers. As illustrated in Fig. 5(a), Transducer 1 serves the transmitter while Transducer 2 acts as the receiver, positioned at opposite ends of the dielectric-metal surface. A copper plate with a thickness of $h_m = 0.05\,\text{mm}$ is employed as the metal ground.

To investigate the impact of different dielectric layers on surface wave propagation, low-loss Polytetrafluoroethylene (PTFE) ($\varepsilon_{r1} = 1.8$, $\tan\delta = 0.00005$ at 26 GHz)[3] and lossy PTFE ($\varepsilon_{r2} = 2.1$, $\tan\delta = 0.0002$ at 26 GHz) are chosen as

[3]Dielectric loss, the imaginary part of the dielectric constant, of a dielectric material is represented by $j\varepsilon_0\varepsilon_r\tan\delta$ with ε_0 being the permittivity of free space and ε_r being the relative permittivity, which indicates the energy loss converted into heat when the material is subjected to an electromagnetic field. By analyzing the propagation constant γ_p of the electromagnetic field, the loss tangent $\tan\delta$ dictates the magnitude of the E-field strength. That is, materials with higher dielectric loss tangent factors experience greater attenuation in E-field strength due to more dielectric losses [4], [40].

the dielectric layers. For a fair comparison, their thicknesses are set to $h_{d1} = 2.95\,\mathrm{mm}$ and $h_{d2} = 2.50\,\mathrm{mm}$ to achieve the same surface impedance Z_s of $j270\,\Omega$. This impedance value can theoretically enhance the excitation efficiency of surface waves [41]. Additionally, two parallel metal walls with a width of $w_w = 1\,\mathrm{mm}$ are integrated into the surface to guide the propagation of surface waves. Different wall materials, including perfect electric conductor (PEC, $\sigma_p = \infty$), copper ($\sigma_c = 59.6 \times 10^6$ S/m), and Galinstan (as fluid metal, $\sigma_g = 3.46 \times 10^6$ S/m), are investigated to examine their influence on the surface wave propagation.

We consider three pathway widths: $9\,\mathrm{mm}$, $11\,\mathrm{mm}$ and $13\,\mathrm{mm}$. The E_x values are measured using multiple sampling probes along the central axis in the $+z$-direction of the propagation pathway. In short-distance transmission, the measured range, referred to as the propagation distance d, spans from $100\,\mathrm{mm}$ to $2000\,\mathrm{mm}$ ($2\,\mathrm{m}$), with the position at $100\,\mathrm{mm}$ serving as the normalized reference point, while in long-distance transmission, the propagation distance ranges from $0.1\,\mathrm{m}$ to $50\,\mathrm{m}$. Note that the E-field strength at the normalized point is set to $0\,\mathrm{dBm}$. As the propagation distance increases from this reference point, the E-field strength diminishes, resulting in negative values. This decline reflects the propagation losses. In subsequent results, the y-axis, representing the E-field strength in dB, predominantly shows negative values. The parameter values used in the simulations are summarized in Table I.

A. Inside Pathway in Short-Distance Transmission

In Fig. 5, we present simulation results for a range of surface configurations, demonstrating the propagation characteristics of surface waves in a surface composed of surface-only, Galinstan wall pathway, and Galinstan pin pathway (the porous surface platform in [34]). The surface-only model in Fig. 5(b) shows the diffusion of surface waves across the entire surface, accompanied by a gradual attenuation of the field strength magnitude as the propagation distance d increases. In contrast, Fig. 5(c) demonstrates that the pathway formed by Galinstan walls effectively concentrates the propagation of surface waves within the pathway while preventing their transmission beyond the Galinstan walls. Similarly, the pathway composed of Galinstan pins exhibits comparable behavior as seen in Fig. 5(d). These findings highlight the similar electromagnetic interaction between solid metal walls and metal pin pathway.

Fig. 6(a) illustrates the simulated values of E_x obtained from the sampling probes along the PEC, copper, and Galinstan wall pathways in the low-loss PTFE surface. Numerical results of the analytical ray tracing model are also presented for comparison. The results from simulations indicate that at a distance of $2000\,\mathrm{mm}$ (corresponding to $173.3\,\lambda$ at the operating frequency of $26\,\mathrm{GHz}$), the surface wave in the Galinstan wall pathway (with electrical conductivity $\sigma_g = 3.46 \times 10^6\,\mathrm{S/m}$) experiences only a loss of $1.6\,\mathrm{dB}$, resulting in a path loss of $0.8\,\mathrm{dB/m}$. Meanwhile, PEC walls ($\sigma_p = \infty$) results in a path loss of $0.5\,\mathrm{dB/m}$, and copper walls ($\sigma_c = 59.6 \times 10^6$ S/m) leads to a path loss of $0.6\,\mathrm{dB/m}$. It is evident that the path loss of the surface wave in the pathway is inversely proportional to the electrical conductivity

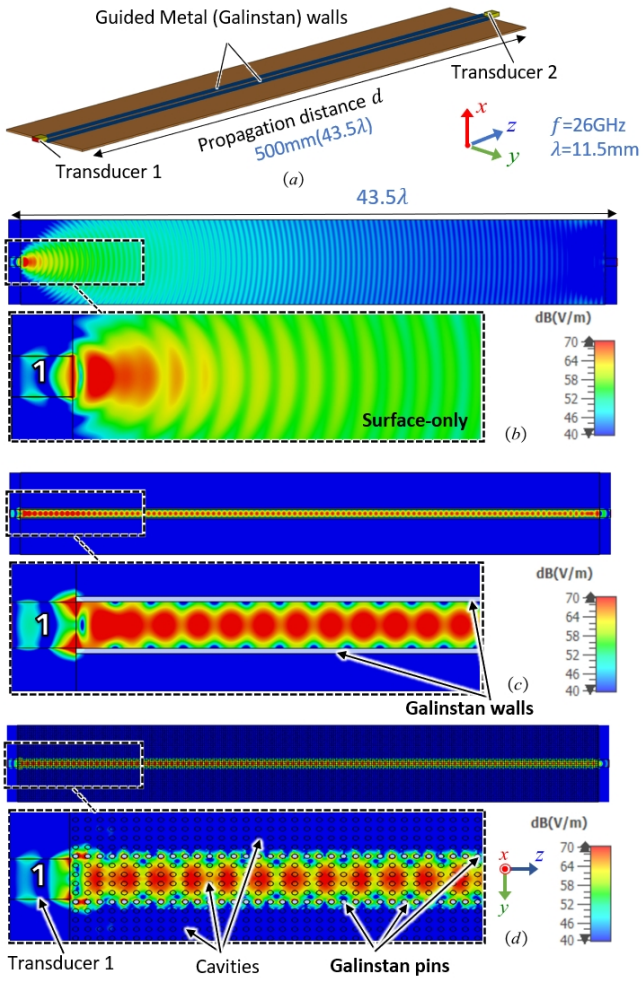

Fig. 5. (a) A surface geometry featuring the guided metal walls and the simulation results for a range of surface configuration models including; (b) surface-only, (c) Galinstan wall pathway, and (d) Galinstan pin pathway.

TABLE I
PARAMETERS USED IN ANALYTICAL MODELS AND SIMULATIONS

Parameter	Value
Operating frequency, f	$26\,\mathrm{GHz}$
Transducer (WR-34) frequency band, f_b	$22 - 33\,\mathrm{GHz}$
Height of transducer aperture, h_a	$4.318\,\mathrm{mm}$
Width of transducer aperture, w_a	$8.636\,\mathrm{mm}$
Relative permittivity of the dielectric layer, ε_r	1.8 , 2.1
Thickness of the dielectric layer, h_d	$2.95\,\mathrm{mm}, 2.50\,\mathrm{mm}$
Surface impedance, Z_s	$j270\,\Omega$
Loss tangent, $\tan\delta$	0.00005, 0.0002
Pathway width, w_p	$9, 11, 13\,\mathrm{mm}$
Thickness of the metal ground, h_m	$0.05\,\mathrm{mm}$
Length of the metal wall, l_w	same with d
Width of the metal wall, w_w	$1\,\mathrm{mm}$
Time of reflection, n	10000
Tilted angle, θ_0	$5°$
Propagation distance, d	$100 - 2000\,\mathrm{mm}$, $0.1 - 50\,\mathrm{m}$
Radius of cavities/ metal pins, r	$0.5\,\mathrm{mm}$
Cavities center-to-center separation, w_c	$2\,\mathrm{mm}$
Electrical conductivity of PEC, σ_p	∞
Electrical conductivity of copper, σ_c	59.6×10^6 S/m
Electrical conductivity of Galinstan, σ_g	3.46×10^6 S/m
Permittivity of free space, ε_0	8.854×10^{-12} F/m
Permeability of free space, μ_0	$4\pi \times 10^{-7}$ H/m

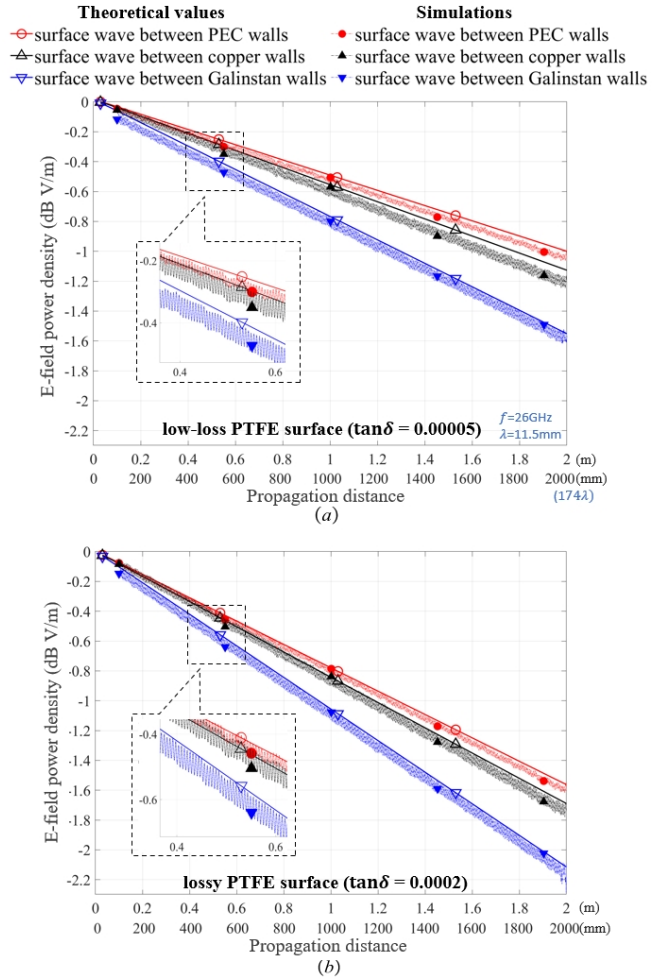

Fig. 6. Numerical and simulation results for surface waves guided by the PEC, copper, and Galinstan wall pathway in the (a) low-loss PTFE surface and (b) lossy PTFE surface within a distance d from $100\,\mathrm{mm}$ to $2000\,\mathrm{mm}$.

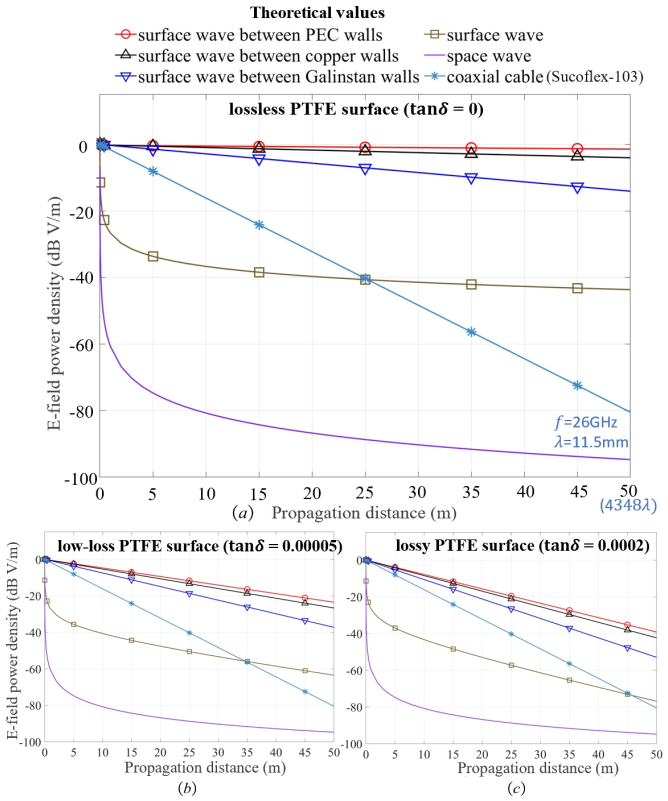

Fig. 7. Numerical results for surface waves within the PEC, copper and Galinstan walls in the (a) lossless PTFE surface with $\tan\delta = 0$, (b) low-loss PTFE surface with $\tan\delta = 0.00005$, and (c) lossy PTFE surface with $\tan\delta = 0.0002$ in long distances. The results for surface wave in the surface-only model, coaxial cable, and space wave are presented for comparison.

of metal walls. Nevertheless, the differences in path losses among the different wall materials are negligible. Therefore, the influence of wall material on path loss can be disregarded for short-distance transmissions. In addition, by comparing Figs. 6(a) and 6(b), it is obvious that the utilization of low-loss tangent PTFE ($\tan\delta = 0.00005$) leads to reduced path loss in each metal wall pathway compared with lossy PTFE ($\tan\delta = 0.0002$). This observation suggests that the selection of a low-loss dielectric layer can effectively reduce path loss.

In the numerical results, it should be noted that the number of reflections, n, is set to 10000 to ensure the convergence of the cumulative E-field strength $E_{x,c}$. It is evident that the numerical values exhibit a slight elevation of up to $0.05\,\mathrm{dB/m}$ compared to the simulation values. This discrepancy can be attributed to the presence of standing waves in the simulation, which leads to a slightly lower field strength. Additionally, in the simulation environment, the transducers deviate from the ideal point sources described in the surface wave ray tracing model, resulting in minor disparities between the two sets of results. However, these discrepancies are deemed negligible.

Moreover, we see that the numerical results match closely with the simulation results, thus validating the effectiveness of the ray tracing model and the accuracy of the derivations. This validation ensures that the model can be used to predict the surface wave path loss at various scales, particularly over long distances, as discussed in Section III-B where simulations are conducted up to $50\,\mathrm{m}$. It is noted that current simulation software, such as CST, often faces challenges in providing precise outcomes in scenarios involving long-distance propagation. In some cases, these software may even fail to produce results in a simulated environment with extensive distances. Furthermore, the utilization of mathematical calculation tools like matrix laboratory (MATLAB) enables nearly instantaneous computation time for the ray tracing model, while performing equivalent simulations in CST to obtain similar results would require a much longer duration (e.g., days). This highlights the advantages associated with the adoption of the surface wave ray tracing model presented in this paper.

B. Inside Pathway in Long-Distance Transmission

Fig. 7 presents the numerical E-field values of the PEC, copper, and Galinstan wall pathways across a range of long-distance transmissions, spanning from $0.1\,\mathrm{m}$ to $50\,\mathrm{m}$. As depicted in Fig. 7(a), when ideal low-loss PTFE ($\tan\delta = 0$) is

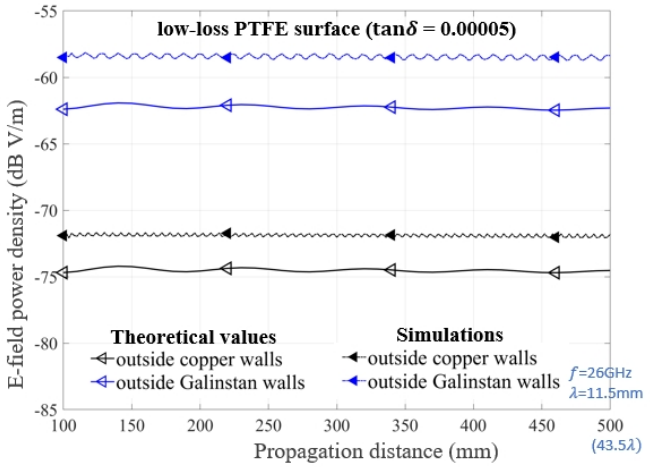

Fig. 8. Numerical and simulation results for surface waves beyond the copper and Galinstan wall pathways with a titled angle $\theta_0 = 5^\circ$ in $500\,\mathrm{mm}$.

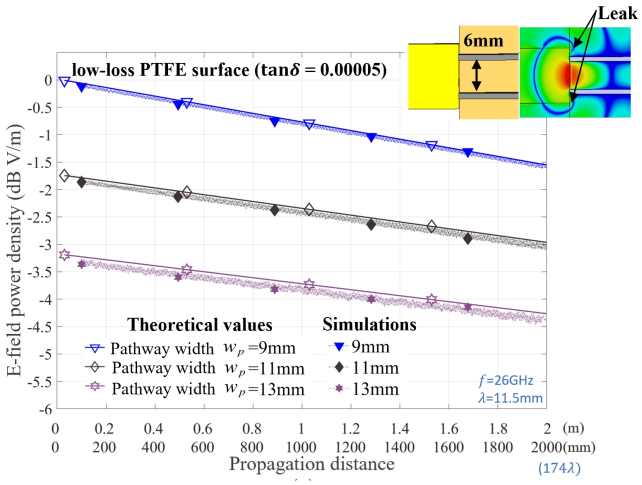

Fig. 9. The numerical and simulation results for surface waves with a pathway width of (a) $w_p = 9\,\mathrm{mm}$, (b) $w_p = 11\,\mathrm{mm}$, and (c) $w_p = 13\,\mathrm{mm}$.

used as the dielectric layer, the E-field attenuation within the PEC, copper, and Galinstan wall pathways is approximately $-1\,\mathrm{dB}$, $-4\,\mathrm{dB}$, and $-14\,\mathrm{dB}$ at $50\,\mathrm{m}$, respectively. Also, the surface-only model, which considers only surface waves, shows an E-field attenuation of $44\,\mathrm{dB}$. In contrast, the attenuation of coaxial cable and space waves are more pronounced, exceeding $80\,\mathrm{dB}$. Note that the surface-only structure refers to a dielectric-metal flat configuration without metal walls. The dielectric used is PTFE with different loss tangents, while the metal ground is copper, as illustrated in Figs. 1 and 5(b). Note that this structure was also used in existing literature [35].

Figs. 7(b) and 7(c) compare the numerical E-field values based on low-loss ($\tan\delta = 0.0005$) and lossy PTFE ($\tan\delta = 0.00002$), respectively. It is worth noting that the loss tangent $\tan\delta$ of these three materials differ. It is evident that the metal walls still provide significant gains. However, as the propagation distance increases, the path loss becomes notably higher and can no longer be neglected as in the short-distance scenarios. Nevertheless, the path loss within the surface wave pathway remains significantly lower as compared to coaxial cable and space wave propagation. In short, the consistency between the predictions of the surface wave ray tracing model and the simulation results, along with its performance in long-distance transmission scenarios, validates that the metal wall pathway has the ability to achieve much lower propagation losses compared to other transmission methods.

C. Outside Pathway in Short-Distance Transmission

Fig. 8 presents the numerical and simulation results where the measured point or sampling probe is positioned outside the metal walls. The tilted angle is 5°. The simulations reveal that the E-field values outside the copper wall pathway are approximately $-71\,\mathrm{dB}$, while the values for the Galinstan walls are around $-58\,\mathrm{dB}$. Notably, the field strength values outside the pathway are significantly lower, exhibiting a difference of approximately $50\,\mathrm{dB}$ compared to the values within the pathway. This observation highlights the metal wall's capability to effectively concentrate the surface wave propagation, resulting in notable gains along the guided pathway.

The significant attenuation of the surface wave signal on the outer surface of the copper wall underscores its strong shielding capability. In contrast, the Galinstan wall, with its lower electrical conductivity, demonstrates a relatively higher level of surface wave leakage. This indicates the potential to select wall materials based on specific application requirements, enabling the achievement of either complete blockage or controlled leakage of surface waves.

Furthermore, it is worth mentioning that the numerical results are slightly lower, approximately $3\,\mathrm{dB}$, compared to the simulation results. This discrepancy can be attributed to the consideration of wave reflections in the simulations, leading to an increase in received power at the receiver. In short, these findings provide evidence for the practical feasibility and utility of metal walls in effectively preventing surface wave propagation in undesired directions. This ensures that the desired signal propagates effectively in the pathway, while minimizing the potential interference outside the pathway.

D. Effect of Pathway Width

As demonstrated in Fig. 9, the pathway width, w_p, between the metal walls also affects the surface wave propagation to a certain extent. In particular, surface waves of various pathway widths experience a similar linear attenuation effect ranging from $100\,\mathrm{mm}$ to $2000\,\mathrm{mm}$, with their E-field values being attenuated by approximately $1.5\,\mathrm{dB}$. However, the key distinction lies in their initial E-field values. For example, with $w_p = 9\,\mathrm{mm}$, the initial E-field value is set to $0\,\mathrm{dB}$, which acts as the normalized reference point. When $w_p = 11\,\mathrm{mm}$, the initial E-field value decreases to $-1.7\,\mathrm{dB}$, and when $w_p = 13\,\mathrm{mm}$, the initial E-field value decreases to $-3.3\,\mathrm{dB}$. These findings demonstrate that narrower pathways effectively concentrate surface wave propagation, thereby mitigating the initial attenuation at the starting position. This behavior arises due to the confinement of surface waves within narrower

pathways, resulting in more focused propagation. However, it is important to note that excessively reducing the pathway width is not a feasible strategy for achieving higher gains within the pathway. As appended in Fig. 9, a pathway width smaller than the transducer aperture width results in surface wave leakage into the outer field, preventing the complete concentration of surface wave energy within the pathway and reducing the E-field strength. Therefore, we recommend selecting a pathway width as close as possible to the transducer aperture width. An optimal pathway width, ideally approximating or slightly exceeding the transducer aperture width denoted as w_a, ensures concentrated surface wave propagation while minimizing excessive attenuation losses.

E. Effect of Metal Wall and Metal Pin Pathways

Fig. 10 illustrates the E-field decay characteristics in Galinstan wall pathways and Galinstan pin pathways using low-loss PTFE and lossy PTFE surfaces. As seen, the E-field values obtained from the simulations align well with the analytical ray-tracing model with metal walls, confirming the effectiveness of the surface wave ray tracing model in accurately capturing path loss within the reconfigurable surface pathways. This suggests that the proposed ray tracing model can also be used to simulate scenarios involving the utilization of liquid metal-filled cavities to achieve reconfigurable surface pathways. In the case of low-loss PTFE, it is observed that the path loss in Galinstan pin pathways with cavities is approximately $1.70\,\mathrm{dB}$ over a propagation distance of $2000\,\mathrm{mm}$, exhibiting a slight increase of approximately $0.15\,\mathrm{dB}$ compared to the path loss in Galinstan wall pathways of approximately $1.55\,\mathrm{dB}$. This difference can be attributed to minor leakage of surface waves beyond the pathway boundaries due to gaps between the cavities in this reconfigurable surface wave platform. Nevertheless, the difference is negligible and can be disregarded. Similar trends can be observed in the case of lossy PTFE. It is important to highlight that metal pin walls present substantial promise in reconfigurable surfaces, facilitated by the dynamic injection of liquid metal into cavities to manipulate surface wave propagation directions. However, the electromagnetic analysis of metal pin walls is inherently intricate. Our proposed model offers an approximate calculation of electromagnetic field intensity in metal pin wall configurations, thereby providing robust reference support for assessing surface wave characteristics on reconfigurable surfaces.

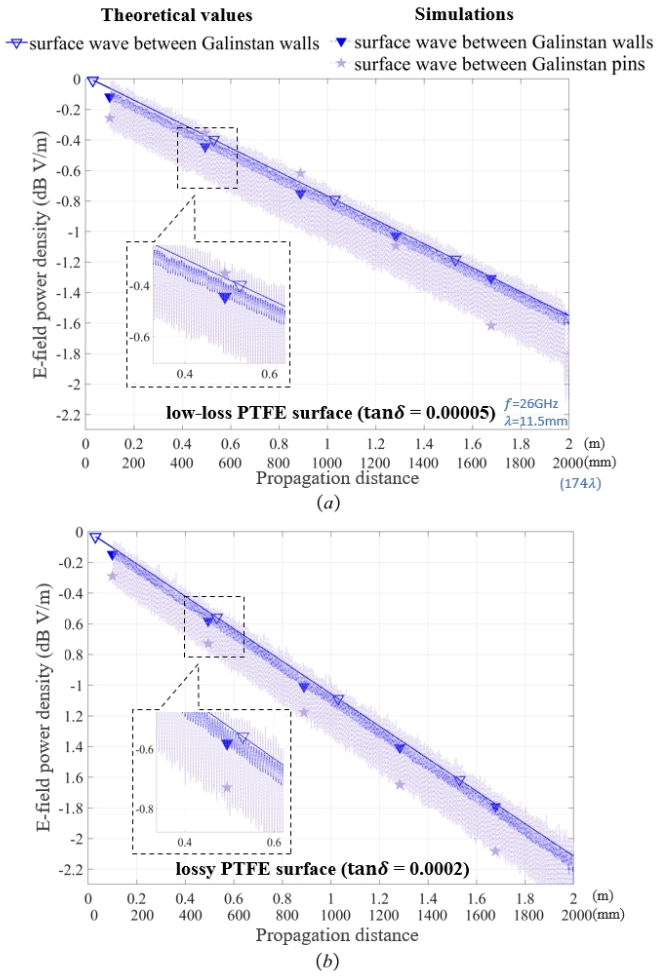

Fig. 10. The numerical and simulation results for surface waves using Galinstan wall or Galinstan pin pathway in the (a) low-loss PTFE surface and (b) lossy PTFE surface.

IV. Conclusions

This paper introduced a novel analytical ray tracing model designed to accurately estimate the electromagnetic field and path loss of surface waves within reconfigurable surface structures. Our proposed model accounts for the effects of E-field superposition and surface material properties, including loss tangent, dielectric constant, and pathway width. Diverging from traditional simulations, our analytical model offers swift computation of surface wave electromagnetic fields. Through validation via extensive simulation, we confirmed the model's accuracy in short-distance propagation scenarios, paving the way for its evaluation in long-distance scenarios that typically are challenging to simulate. Our numerical findings underscore the superiority of SWC over coaxial cable and space-wave communications in minimizing path loss. Furthermore, our work delves into optimal designs of reconfigurable structures by examining the impacts of various factors such as dielectric layers, wall materials, leakage, and pathway width. Intriguingly, our model has also extended its predictive capabilities to anticipate the electromagnetic field behavior of metal pins embedded within reconfigurable surfaces. Using the proposed model and insights presented in this paper, future research endeavors in SWC could focus on performance analysis.

References

[1] F. R. Ghadi *et al.*, "On performance of RIS-aided fluid antenna systems," *IEEE Wireless Commun. Lett.*, early access, DOI:10.1109/LWC.2024.3405636, May 2024.

[2] E. Basar and H. V. Poor, "Present and future of reconfigurable intelligent surface-empowered communications," *IEEE Sig. Proc. Mag.*, vol. 38, no. 6, pp. 146-152, Nov. 2021.

[3] K. K. Wong, K. F. Tong, Z. Chu and Y. Zhang, "A vision to smart radio environment: Surface wave communication superhighways," *IEEE Wireless Commun.*, vol. 28, no. 1, pp. 112-119, Feb. 2021.

[4] H. Barlow, "Surface waves," *Proc. IRE*, vol. 46, no. 7, pp. 1413–1417, 1958.

[5] H. Barlow and A. Karbowiak, "An investigation of the characteristics of cylindrical surface waves," in *Proc. IEE–Part III: Radio & Commun. Eng.*, vol. 100, no. 68, pp. 321–328, 1953.

[6] A. J. Karkar *et al.*, "Hybrid wire-surface wave interconnects for next-generation networks-on-chip," *IET Computers & Digital Tech.*, vol. 7, no. 6, pp. 294–303, 2013.

[7] A. Karkar, N. Dahir, T. Mak, and K.-F. Tong, "Thermal and performance efficient on-chip surface-wave communication for many-core systems in dark silicon era," *ACM J. Emerging Technol. Comput. Syst.*, vol. 18, no. 3, pp. 1–18, 2022.

[8] L. Berkelmann and D. Manteuffel, "Antenna parameters for on-body communications with wearable and implantable antennas," *IEEE Trans. Antennas & Propag.*, vol. 69, no. 9, pp. 5377–5387, Sept. 2021.

[9] H. Wang, Y. Shen, K. F. Tong, and K. K. Wong, "Continuous electrowetting surface-wave fluid antenna for mobile communications," in *Proc. IEEE TENCON*, 1-4 Nov. 2022, Hong Kong SAR, China.

[10] Y. Shen *et al.*, "Design and implementation of mmWave surface wave enabled fluid antennas and experimental results for fluid antenna multiple access," *arXiv preprint*, arXiv:2405.09663, May 2024.

[11] J. O. Martínez *et al.*, "Toward liquid reconfigurable antenna arrays for wireless communications," *IEEE Commun. Mag.*, vol. 60, no. 12, pp. 145–151, Dec. 2022.

[12] W. K. New, K. K. Wong, H. Xu, K. F. Tong and C.-B. Chae, "An information-theoretic characterization of MIMO-FAS: Optimization, diversity-multiplexing tradeoff and q-outage capacity," *IEEE Trans. Wireless Commun.*, vol. 23, no. 6, pp. 5541–5556, Jun. 2024.

[13] C. Wang *et al.*, "Fluid antenna system liberating multiuser MIMO for ISAC via deep reinforcement learning," *IEEE Trans. Wireless Commun.*, early access, DOI:10.1109/TWC.2024.3376800, Mar. 2024.

[14] J. Turner and M. Jessup, "How surface waves reduce through-life costs," *Measurement and Control*, vol. 46, no. 6, pp. 180–184, 2013.

[15] H. M. Barlow and J. Brown, *Radio surface waves*. Clarendon Press, 1962.

[16] H. Barlow and A. E. Karbowiak, "An experimental investigation of the properties of corrugated cylindrical surface waveguides," *Proc. IEE–Part III: Radio & Commun. Eng.*, vol. 101, no. 71, pp. 182–188, 1954.

[17] M. Hayes and R. Rivlin, "Surface waves in deformed elastic materials," *Archive for Rational Mechanics and Analysis*, vol. 8, pp. 358–380, 1961.

[18] E. Johansen, "Surface wave scattering by a step," *IEEE Trans. Antennas & Propag.*, vol. 15, no. 3, pp. 442–448, 1967.

[19] A. Shojaeifard *et al.*, "MIMO evolution beyond 5G through reconfigurable intelligent surfaces and fluid antenna systems," *Proc. IEEE*, vol. 110, no. 9, pp. 1244–1265, Sept. 2022.

[20] S. Sun *et al.*, "High-efficiency broadband anomalous reflection by gradient meta-surfaces," *Nano Lett.*, vol. 12, no. 12, pp. 6223–6229, 2012.

[21] Z. Sun, X. Zuo, T. Guan, and W. Chen, "Artificial TE-mode surface waves at metal surfaces mimicking surface plasmons," *Optics Express*, vol. 22, no. 4, pp. 4714–4722, 2014.

[22] Y. Liu *et al.*, "Simultaneous manipulation of electric and magnetic surface waves by topological hyperbolic metasurfaces," *ACS Applied Elect. Materials*, vol. 3, no. 9, pp. 4203–4209, 2021.

[23] R. Mitchell-Thomas, T. McManus, O. Quevedo-Teruel, S. Horsley, and Y. Hao, "Perfect surface wave cloaks," *Physical Review Lett.*, vol. 111, no. 21, p. 213901, 2013.

[24] T. McManus, J. Valiente-Kroon, S. Horsley, and Y. Hao, "Illusions and cloaks for surface waves," *Scientific Reports*, vol. 4, no. 1, p. 5977, 2014.

[25] T. McManus, L. La Spada, and Y. Hao, "Isotropic and anisotropic surface wave cloaking techniques," *J. Optics*, vol. 18, no. 4, p. 044005, 2016.

[26] S. Xu *et al.*, "Broadband surface-wave transformation cloak," *Proc. National Academy Sci.*, vol. 112, no. 25, pp. 7635–7638, 2015.

[27] L. Jing, B. Zheng, S. Xu, L. Shen, and H. Chen, "Experimental study on invisibility cloaks," in *Proc. IEEE Inter. Workshop Electromag.: Appl. & Student Innovation Competition*, 2016.

[28] S. Tcvetkova, D.-H. Kwon, A. Diaz-Rubio, and S. Tretyakov, "Nearly perfect conversion of a propagating wave into a surface wave," in *Proc. IEEE Inter. Conf. Electromag. Adv. Appl.*, pp. 1426–1428, 2017.

[29] S. Tcvetkova, D.-H. Kwon, A. Díaz-Rubio, and S. Tretyakov, "Near-perfect conversion of a propagating plane wave into a surface wave using metasurfaces," *Physical Review B*, vol. 97, no. 11, p. 115447, 2018.

[30] V. Popov *et al.*, "Omega-bianisotropic metasurface for converting a propagating wave into a surface wave," *Physical Review B*, vol. 100, no. 12, p. 125103, 2019.

[31] S. Tcvetkova, E. Martini, S. Tretyakov, and S. Maci, "Perfect conversion of a TM surface wave into a TM leaky wave by an isotropic periodic metasurface printed on a grounded dielectric slab," *IEEE Trans. Antennas & Propag.*, vol. 68, no. 8, pp. 6145–6153, Aug. 2020.

[32] S. Tcvetkova, S. Maci, and S. Tretyakov, "Exact solution for conversion of surface waves to space waves by periodical impenetrable metasurfaces," *IEEE Trans. Antennas & Propag.*, vol. 67, no. 5, pp. 3200–3207, May 2019.

[33] B. Liang and M. Bai, "Subwavelength three-dimensional frequency selective surface based on surface wave tunneling," *Optics Express*, vol. 24, no. 13, pp. 14 697–14 702, 2016.

[34] Z. Chu, K. K. Wong, and K. F. Tong, "Reconfigurable surface wave platform using fluidic conductive structures," in *Proc. IEEE Inter. Symp. Antennas & Propag. and USNC-URSI Radio Sci. Meeting*, pp. 909–910, 4-10 Dec. 2021, Singapore.

[35] Z. Chu, K. F. Tong, K. K. Wong, C. B. Chae, and Y. Zhang, "Partitioning surface wave propagation on reconfigurable porous plane," *Scientific Reports*, vol. 14, no. 1, p. 207, Jan. 2024.

[36] T. K. Geok *et al.*, "A comprehensive review of efficient ray-tracing techniques for wireless communication," *Inter. J. Commun. Antenna & Propag.*, vol. 8, no. 2, pp. 123–136, 2018.

[37] J. Zenneck, "Über die Fortpflanzung ebener elektromagnetischer Wellen längs einer ebenen Leiterfläche und ihre Beziehung zur drahtlosen Telegraphie," *Ann. Phys.*, vol. 328, no. 10, pp. 846–866, 1907.

[38] Z. Chu, K.-K. Wong, and K.-F. Tong, "Enhancing and localizing surface wave propagation with reconfigurable surfaces," in *Proc. Inter. Symp. Antennas & Propag.*, 19-22 Oct. 2021, Taipei, Taiwan.

[39] H. Barlow and A. Cullen, "Surface waves," *Proc. IEE–Part III: Radio & Commun. Eng.*, vol. 100, no. 68, pp. 329–341, 1953.

[40] D. K. Ghodgaonkar, V. V. Varadan, and V. K. Varadan, "A free-space method for measurement of dielectric constants and loss tangents at microwave frequencies," *IEEE Trans. Instrum. Meas.*, vol. 38, no. 3, pp. 789–793, Jun. 1989.

[41] J. Wan, K. F. Tong, and C. H. Chan, "Simulation and experimental verification for a 52 GHz wideband trapped surface wave propagation system," *IEEE Trans. Antennas & Propag.*, vol. 67, no. 4, pp. 2158–2166, Apr. 2019.

Zhiyuan Chu (Graduate Student Member, IEEE) received the B.Eng. degree from the Beijing University of Posts and Telecommunications, Beijing, China, in 2017, and the M.Sc. degree (Hons.) from The University of Sheffield, Sheffield, U.K., in 2018. And he received the Ph.D. degree from the Department of Electronic and Electrical Engineering, University College London, London, UK, in 2023. He received the Best Student Paper Award at the 2021 International Symposium on Antennas and Propagation (ISAP).

(Aven) Wee Kiat New (Member, IEEE) received his Ph.D in Electrical Engineering from Universiti Teknologi Malaysia, M.Eng.Sc in Electrical Engineering from University of Malaya and B.IT in Data Communications and Networking from Multimedia University. He was a visiting researcher at Lancaster University and University of Cyprus. He is currently a research fellow at the Department of Electronic and Electrical Engineering, University College London, UK. His research interests are information theory, optimization, stochastic processes, machine learning and their applications in emerging areas of communications. He was the recipient of the 2021 IEEE Malaysia Comsoc/VTS best paper award, 2021 and 2020 IEEE Malaysia AP/MTT/EMC best paper awards.

(Kenneth) Kin-Fai Tong (Fellow, IEEE) (M'99-SM'13-F'23) received the B.Eng. and Ph.D. degrees in electronic engineering from the City University of Hong Kong in 1993 and 1997, respectively. After graduation, Dr. Tong worked in the Department of Electronic Engineering at City University of Hong Kong as a Research Fellow. Two years later, he took up the post Expert researcher in the Photonic Information Technology Group and Millimetre-wave Devices Group at the National Institute of Information and Communications Technology (NiCT), Japan, where his main research focused on photonic-millimeter-wave planar antennas at 10GHz, 38 GHz and 60 GHz for high-speed wireless communications systems. In 2005, he started his academic career in the Department of Electronic and Electrical Engineering, UCL, as a Lecturer. Now Dr. Tong is Chair in Antennas in the department. His current research interests include millimeter-wave and THz antennas, fluid antennas, 3D printed antennas and sub-GHz long range IoT networks. He served as the General Co-Chair of the 2017 International Workshop on Electromagnetics (iWEM), and Lead Guest Editor of IEEE OJAP in 2020.

(Kit) Kai-Kit Wong (Fellow, IEEE) (M'01-SM'08-F'16) received the BEng, the MPhil, and the PhD degrees, all in Electrical and Electronic Engineering, from the Hong Kong University of Science and Technology, Hong Kong, in 1996, 1998, and 2001, respectively. He is Chair in Wireless Communications at the Department of Electronic and Electrical Engineering, University College London, UK. His current research centers around 6G and beyond mobile communications. He is Fellow of IEEE and IET and is also on the editorial board of several international journals. He served as the Editor-in-Chief for IEEE Wireless Communications Letters between 2020 and 2023.

Haizhe Liu received the B.Eng. degree in Automation and the M.Sc. degree in System Engineering from the North China Electric Power University, China, in 2016 and 2019, respectively. She is currently a Ph.D. student at the Department of Electronic and Electrical Engineering, University College London, UK. Her research interests mainly include MIMO systems, surface wave and metasurface materials in 5G and beyond wireless communications.

Chan-Byoung Chae (Fellow, IEEE) received the Ph.D. degree in electrical and computer engineering from The University of Texas at Austin (UT), USA in 2008, where he was a member of wireless networking and communications group (WNCG).

Prior to joining UT, he was a Research Engineer at the Telecommunications R&D Center, Samsung Electronics, Suwon, South Korea, from 2001 to 2005. He is currently an Underwood Distinguished Professor with the School of Integrated Technology, Yonsei University, South Korea. Before joining Yonsei University, he was with Bell Labs, Alcatel-Lucent, Murray Hill, NJ, USA, from 2009 to 2011, as a Member of Technical Staff, and Harvard University, Cambridge, MA, USA, from 2008 to 2009, as a Post-Doc. Research Fellow.

Dr. Chae was a recipient/co-recipient of the Ministry of Education Award in 2024, the KICS Haedong Scholar Award in 2023, the CES Innovation Award in 2023, the IEEE ICC Best Demo Award in 2022, the IEEE WCNC Best Demo Award in 2020, the Best Young Engineer Award from the National Academy of Engineering of Korea (NAEK) in 2019, the IEEE DySPAN Best Demo Award in 2018, the IEEE/KICS Journal of Communications and Networks Best Paper Award in 2018, the IEEE INFOCOM Best Demo Award in 2015, the IEIE/IEEE Joint Award for Young IT Engineer of the Year in 2014, the KICS Haedong Young Scholar Award in 2013, the IEEE Signal Processing Magazine Best Paper Award in 2013, the IEEE ComSoc AP Outstanding Young Researcher Award in 2012, and the IEEE VTS Dan. E. Noble Fellowship Award in 2008.

Dr. Chae has held several editorial positions, including Editor-in-Chief of the IEEE Transactions on Molecular, Biological, and Multi-Scale Communications, Senior Editor of the IEEE Wireless Communications Letters, and Editor for the IEEE Communications Magazine, IEEE Transactions on Wireless Communications, and IEEE Wireless Communications Letters. He was an IEEE ComSoc Distinguished Lecturer from 2020 to 2023 and is an IEEE VTS Distinguished Lecturer from 2024 to 2025. He is an IEEE Fellow and elected member of the National Academy of Engineering of Korea.

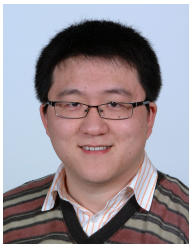

Yangyang Zhang received the B.S. and M.S. degrees in electronics and information engineering from Northeastern University, Shenyang, China, in 2002 and 2004 respectively, and the Ph.D. degree in electrical engineering from the University of Oxford, Oxford, U.K., in 2008. He is Director of Kuang-Chi Science Limited, Hong Kong. His research interests include multiple-input multiple-output wireless communications and stochastic optimization algorithms. Dr. Zhang has been awarded more than 20 honours. Besides, he also authored and co-authored more than 50 refereed papers.